Central-moment discrete Boltzmann method for reactive flows

Xianli Su[a,b], Chuandong Lin[a,c,d,*], Linlin Fei[e], KaiHong Luo[b]

[a]*Sino-French Institute of Nuclear Engineering and Technology, Sun Yat-sen University, Zhuhai, 519082, Guangdong, China*
[b]*Department of Mechanical Engineering, University College London, Torrington Place, London, WC1E 7JE, United Kingdom*
[c]*Key Laboratory for Thermal Science and Power Engineering of Ministry of Education, Department of Energy and Power Engineering, Tsinghua University, Beijing, 100084, China*
[d]*National University of Singapore, Department of Mechanical Engineering, National University of Singapore, 119077, Singapore*
[e]*Chair of Building Physics, Department of Mechanical and Process Engineering, ETH Zürich, (Swiss Federal Institute of Technology in Zürich), Zürich, 8092, Switzerland*

Abstract

A central-moment discrete Boltzmann method (CDBM) is proposed for reactive flows, accommodating adjustable specific heat ratios and Prandtl numbers. In the framework of CDBM, a unified set of kinetic equations is used to delineate both macroscopic quantities and higher-order central moments. Via these central moments, the nonequilibrium effects that are directly related to the thermal fluctuation beyond conventional hydrodynamic governing equations can be quantified. Moreover, the discrete Boltzmann equation of the CDBM is simpler than that of previous multiple-relaxation-time DBMs, owing to the elimination of the additional term in the DBM. Furthermore, this method is capable of modeling supersonic compressible reactive flows characterized by high Mach numbers. The model is verified through simulations encompassing sound waves, shock waves, thermal Couette flows, regular shock reflections, and supersonic reactive waves.

Keywords: Reactive flows, nonequilibrium effects, central-moment discrete Boltzmann method

*Corresponding author
Email address: linchd3@mail.sysu.edu.cn (Chuandong Lin)

1. Introduction

Reactive flows refer to fluid flows with chemical reactions which include a broad range of phenomena, such as flames, detonations, chemical lasers and the earth's atmosphere. Applications can be found in the field of transportation, energy generation and materials processing [1]. The research on reactive flows is also a key issue to change the atmospheric pollution, climate change and global warming which are directly relevant to harmful emissions from reactive flows. However, reactive flows are known to be a challenge for numerical simulations due to a large number of coupled physicochemical processes and scales both in time and space [1, 2]. All of the processes, such as the chemical reactions, subsequent heat release, and the fluid dynamics, must be considered simultaneously [1, 2]. In addition, the influence of hydrodynamic and thermodynamic nonequilibrium effects are significant around sharp physical gradients, which are common in violent reacting flows. This increases the complexity of the problem and the difficulty of research, because the nonequilibrium effects always change density, velocity, temperature, etc., in the evolution of fluid systems away from equilibrium, especially in transient and/or extreme conditions [3, 4].

Serving as the cornerstone of kinetic theory, the Boltzmann equation provides the potential to effectively and accurately simulate intricate nonequilibrium flows across a broad spectrum of spatiotemporal scales. In 1997, Succi et al. established the first lattice Boltzmann model (LBM) applied to reactive flows and successfully simulated the methane/air diffusion flame problem in the limit of fast chemistry [5]. Since then, and up until the late 2010s, there are some progress of LBM in combustion research [6, 7, 8, 9, 10, 11], but all limited to a simplified case in the absence of a good compressible realization, persistent issues with stability of solvers and the absence of multi-species formulations [12]. As a promising kinetic method, remarkable progresses have been made by using LBM in recent years. For example, in 2019, Hosseini et al. proposed a hybrid lattice Boltzmann-finite difference numerical scheme for the simulation of reacting flows at low Mach number and simulated three-dimensional counter-flow premixed flame [13]. In 2022, Sawant et al. proposed a LBM for compressible reacting multi-species flows recovering the Stefan–Maxwell diffusion closure together with barodiffusion [14]. In 2023, a new finite-volume schemes based on the LBM for simulations of

gaseous detonations have been proposed by Gauthier et al. [15]. Despite their progress, most LBMs for combustion are limited to low Mach number reactive flows and all ignore a variety of thermodynamic nonequilibrium effects included in the Boltzmann equation.

In parallel with efforts to develop standard LBMs for reactive flows simulations, other attempts at developing Boltzmann-based models have also made progress, such as discrete Boltzmann method (DBM), which has been developed and successfully used in various complex systems [16, 17, 18, 19, 20, 21, 22]. In particular, the DBM introduces higher-order kinetic moments so that hydrodynamic and thermodynamic fields are fully coupled, macroscopic equations can be recovered accurately [23]. Furthermore, the DBM can bring deeper insights into the hydrodynamic and thermodynamic nonequilibrium effects beyond the Navier-Stokes (NS) equations[23]. In 2012, Xu et al. first proposed the idea that the physical quantities and nonequilibrium information of a system can be described and extracted with the help of kinetic moments of distribution functions [24]. In 2013, Yan et al. were pioneers in proposing a DBM for detonations, employing the Lee-Traver reaction model [25]. In 2014, Lin et al. introduced a DBM in polar coordinate system to probe the implosion and explosion processes, in which the Cochran rate function was invoked to describe the chemical process [26]. In 2015, Xu et al. developed a two-dimensional multi-relaxation DBM that achieved the natural coupling of heat release from chemical reactions with fluid systems [27]. In 2016, through the Chapman–Enskog multiscale analysis, Zhang et al. determined the physical meanings of the nonequilibrium quantities in the DBM [28]. In 2021, Ji et al. developed a DBM to a three-dimensional supersonic reaction flow system and successfully simulated the unstable detonation phenomenon [29]. In 2023, Su et al. obtained and analyzed the characteristics of unsteady detonation by using the DBM [22]. In 2024, Ji et al. proposed an eulerian discrete kinetic framework in comoving reference frame to simulate hypersonic compressible flows [30].

In this paper, we develop a robust and accurate central-moment discrete Boltzmann method (CDBM) for reactive flows with flexible specific heat ratios and Prandtl numbers. The "central-moment-based" was firstly proposed in LBM for a cascaded operator, conducting collisions in the central-moment space [31, 32, 33]. Then Zhang et al. employed a central-moment-based multiple relaxation time collision operator in discrete unified gas kinetic scheme for incompressible two-phase flows [34].Inspired by existing works, we employ central moments based on peculiar velocity to compute discrete equilibrium

distribution functions, collision terms, and reaction terms, whereas all preceding DBMs are formulated in raw-moment space. During the recovery of traditional Navier-Stokes (NS) equations through the Chapman-Enskog expansion, it is discovered that the collision term of all DBMs necessitates modification with an additional term to restore the lost relationship in the process of coarse-grained modeling. However, the additional term can be eliminated in the CDBM, which is naturally consistent with the NS equations in the hydrodynamic limit. Furthermore, nonequilibrium effects captured by DBMs are rooted in raw moments, implying their correlation with the coupled behaviors of flow and thermal. In contrast, the CDBM possesses the capability to directly quantify the nonequilibrium effects of reactive flows associated with thermal fluctuations. This aids in examining the mechanisms and characterizations of reactive flows with regard to thermal fluctuations.

The rest of the paper is organized as follows. The CDBM are described in Sec. 2. In Sec. 3, the model is validated by typical benchmarks, i.e., the sound wave, the shock wave, the thermal Couette flow, the regular shock reflection, and the supersonic reactive flow. Finally, conclusions are presented in Sec. 4.

2. Central-moment-based discrete Boltzmann model

In formulating the CDBM, a unified set of equations is employed to concurrently describe macroscopic quantities (e.g., density, velocity, and temperature) and higher-order central moments,

$$\frac{\partial f_i}{\partial t} + \mathbf{v}_i \cdot \nabla f_i = \Omega_i + R_i, \tag{1}$$

where t is the time, $\mathbf{v}_i$ the $i-th$ discrete velocity, f_i the discrete distribution function, and ∇ the Hamilton operator.

It should be noted that the discretization refers to the discretization of the particle velocity distribution function in the velocity space, and the discretization format is flexible. In this paper, we utilize a two-dimensional sixteen-velocity (D2V16) model, depicted in Fig. 1. The discrete velocities and associated parameters are structured as follows,

$$\mathbf{v}_i = \begin{cases} \mathrm{cyc}: v_a\left(\pm 1, 0\right), & 1 \le i \le 4, \\ \mathrm{cyc}: v_b\left(\pm 1, \pm 1\right), & 5 \le i \le 8, \\ \mathrm{cyc}: v_c\left(\pm 1, 0\right), & 9 \le i \le 12, \\ \mathrm{cyc}: v_d\left(\pm 1, \pm 1\right), & 13 \le i \le 16, \end{cases} \tag{2}$$

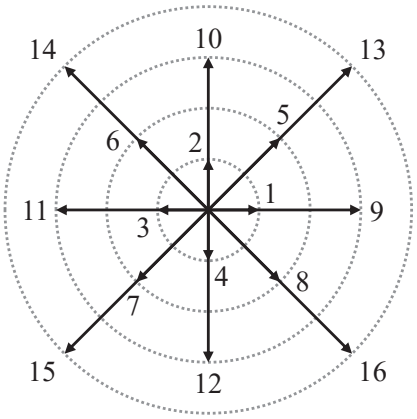

Figure 1: Sketch of discrete velocities.

$$\eta_i = \begin{cases} \eta_a, & 1 \leq i \leq 4, \\ \eta_b, & 5 \leq i \leq 8, \\ \eta_c, & 9 \leq i \leq 12, \\ \eta_d, & 13 \leq i \leq 16, \end{cases} \tag{3}$$

where v_a, v_b, v_c and v_d are tunable parameters controlling the value of discrete velocities, η_a, η_b, η_c and η_d are the corresponding parameters for degrees of freedom, and cyc denotes the cyclic permutation.

On the right side of Eq. 1, Ω_i represents the collision term which accounts for the change rate of distribution function due to molecular collisions and takes the form

$$\Omega_i = -C_{ij}^{-1} S_{jk} \left(\bar{f}_k - \bar{f}_k^{eq} \right), \tag{4}$$

where C_{ij}^{-1} is the element of the transition matrix $\mathbf{C^{-1}} = \left(\mathbf{C}_1^{-1} \ \mathbf{C}_2^{-1} \ \cdots \ \mathbf{C}_{16}^{-1} \right)^{\mathrm{T}}$ containing the blocks $\mathbf{C}_i^{-1} = \left(C_{i1}^{-1} \ C_{i2}^{-1} \ \cdots \ C_{i16}^{-1} \right)$. In fact, the transition matrix serves as the bridge for transformation of velocity distribution function between central moment space and discrete velocity space. The parameter S_{jk} is the element of the matrix $\bar{\mathbf{S}}$= diag $(S_1 \ S_2 \ \cdots \ S_{16})$, which controls the relaxation speed of $\bar{f}_k$ approaching $\bar{f}_k^{eq}$. In addition, $\bar{f}_k$ and $\bar{f}_k^{eq}$ represent discrete distribution function and its equilibrium counterpart in central moment space, respectively. The subscript k is used to mark the central moment. Correspondingly, the Prandtl number is adjustable and reads $\mathrm{Pr} = S_\kappa / S_\mu$, under the conditions $S_5 = S_6 = S_7 = S_\mu$ and $S_8 = S_9 = S_\kappa$. For the purpose of recovering NS equations in the hydrodynamic limit, the equilibrium

discrete distribution function should satisfy the following central moment relationships:

$$\int\int f^{eq}\Psi d\mathbf{v}d\eta=\sum\nolimits_i f_i^{eq}\Psi_i, \tag{5}$$

with $\Psi=1$, $\mathbf{v}^*$, $\mathbf{v}^*\cdot\mathbf{v}^*+\eta^2$, $\mathbf{v}^*\cdot\mathbf{v}^*$, $(\mathbf{v}^*\cdot\mathbf{v}^*+\eta^2)\,\mathbf{v}^*$, $\mathbf{v}^*\mathbf{v}^*\mathbf{v}^*$, $(\mathbf{v}^*\cdot\mathbf{v}^*+\eta^2)\,\mathbf{v}^*\mathbf{v}^*$, correspondingly, $\Psi_i=1$, $\mathbf{v}_i^*$, $\mathbf{v}_i^*\cdot\mathbf{v}_i^*+\eta_i^2$, $\mathbf{v}_i^*\cdot\mathbf{v}_i^*$, $(\mathbf{v}_i^*\cdot\mathbf{v}_i^*+\eta_i^2)\,\mathbf{v}_i^*$, $\mathbf{v}_i^*\mathbf{v}_i^*\mathbf{v}_i^*$, $(\mathbf{v}_i^*\cdot\mathbf{v}_i^*+\eta_i^2)\,\mathbf{v}_i^*\mathbf{v}_i^*$. Here $\mathbf{v}^*=\mathbf{v}-\mathbf{u}$ and $\mathbf{v}_i^*=\mathbf{v}_i-\mathbf{u}$, with $\mathbf{u}$ the flow velocity, η and η_i are used to describe the corresponding vibrational and/or rotational energies. Besides, the equilibrium distribution function f^{eq} takes the form [35]

$$f^{eq}=n\Big(\frac{m}{2\pi T}\Big)^{D/2}\Big(\frac{m}{2\pi IT}\Big)^{1/2}\exp\left[-\frac{m|\mathbf{v}-\mathbf{u}|^2}{2T}-\frac{m\eta^2}{2IT}\right], \tag{6}$$

where n is the particle number density, $m=1$ the particle mass, and $\rho=nm$ the mass density. Besides, T represents the temperature, D denotes the dimension, I stands for extra degrees of freedom due to vibration and/or rotation, and $\gamma=(D+I+2)/(D+I)$ represents the specific heat ratio. The previous central moment relationships can be written into $\bar{f}_k^{eq}=C_{ki}f_i^{eq}$, with $\bar{f}_1^{eq}=\rho$, $\bar{f}_2^{eq}=0$, $\bar{f}_3^{eq}=0$, $\bar{f}_4^{eq}=\rho T\,(I+D)$, $\bar{f}_5^{eq}=\rho T$, $\bar{f}_6^{eq}=0$, $\bar{f}_7^{eq}=\rho T$, $\bar{f}_8^{eq}=0$, $\bar{f}_9^{eq}=0$, $\bar{f}_{10}^{eq}=0$, $\bar{f}_{11}^{eq}=0$, $\bar{f}_{12}^{eq}=0$, $\bar{f}_{13}^{eq}=\rho T^2\,(D+I+2)$, $\bar{f}_{14}^{eq}=0$, $\bar{f}_{15}^{eq}=0$, and $\bar{f}_{16}^{eq}=\rho T^2\,(D+I+2)$. Therefore, the equilibrium discrete distribution function can be calculted by $f_i^{eq}=C_{ik}^{-1}\bar{f}_k^{eq}$.

In addition, the reaction term R_i is the change rate of the discrete distribution function due to the chemical reaction. The original expression reads [36]

$$R=\frac{-\,(1+D)\,IT+I|\mathbf{v}-\mathbf{u}|^2+\eta^2}{2IT^2}f^{eq}T', \tag{7}$$

where $T'=2Q\lambda'/(D+I)$ is the varying rate of temperature, and the superscript $'$ denotes the changing rate due to chemical reaction. Besides, Q and λ indicate the chemical heat release per unit mass of fuel and the mass fraction of chemical product, respectively. Similarly, the reaction term also satisfies the corresponding central moment relationships:

$$\int\int R\Psi d\mathbf{v}d\eta=\sum\nolimits_i R_i\Psi_i, \tag{8}$$

where the elements of Ψ and Ψ_i are identical to those in Eq. (5). Therefore, the reaction term can be calculated by $R_i=C_{il}^{-1}\bar{R}_l$, and $\bar{R}_l$ is the element of matrix $\bar{\mathbf{R}}=\big(\bar{R}_1\ \bar{R}_2\ \cdots\ \bar{R}_N\big)^{\mathrm{T}}$. The detailed expressions are $\bar{R}_1=0$,

$\bar{R}_2 = 0$, $\bar{R}_3 = 0$, $\bar{R}_3 = 0$, $\bar{R}_4 = 2\rho\lambda' Q$, $\bar{R}_5 = 2\rho\lambda' Q/(D+I)$, $\bar{R}_6 = 0$, $\bar{R}_7 = 2\rho\lambda' Q/(D+I)$, $\bar{R}_8 = 0$, $\bar{R}_9 = 0$, $\bar{R}_{10} = 0$, $\bar{R}_{11} = 0$, $\bar{R}_{12} = 0$, $\bar{R}_{13} = 0$, $\hat{R}_{14} = 2\lambda' Q\rho T(D+I+2)/(D+I)$, $\bar{R}_{15} = 0$, and $\hat{R}_{16} = 2\lambda' Q\rho T(D+I+2)/(D+I)$.

It is worth mentioning that the governing equation Eq. 1 is simpler than those of all preceding DBMs, owing to the absence of an additional term. This stems from the fact that traditional NS equations can be directly derived from CDBM through the Chapman-Enskog expansion. Besides, the CDBM contains more detailed nonequilibrium effects than a traditional NS model, as it enables simultaneous determination of density, velocity, temperature, and higher-order kinetic moments. Specifically, adhering to conservation laws, f_i^{eq} can be replaced by f_i in the first three central moment relationships in Eq. 5, from which the density ρ, hydrodynamic velocity $\mathbf{u}$, the energy E, and temperature T can be obtained,

$$\rho = \sum\nolimits_i f_i, \tag{9}$$

$$\rho\mathbf{u} = \sum\nolimits_i f_i \mathbf{v}_i, \tag{10}$$

$$E = \frac{1}{2}\rho\mathbf{u}\cdot\mathbf{u} + \frac{1}{\gamma-1}\rho T = \frac{1}{2}\sum\nolimits_i f_i\left(\mathbf{v}_i\cdot\mathbf{v}_i + \eta^2\right). \tag{11}$$

Nonetheless, substituting f_i^{eq} with f_i introduces a discrepancy between the left and right sides of the last four central moment relationships in Eq. 5. These disparities in higher-order moments of the distribution function from their equilibrium counterparts reflect the deviation of physical system from its equilibrium state. In other words, the CDBM can be employed to quantify the following nonequilibrium manifestations,

$$\mathbf{\Delta}_2^* = \sum\nolimits_i \left(f_i - f_i^{eq}\right)\mathbf{v}_i^*\mathbf{v}_i^*, \tag{12}$$

$$\mathbf{\Delta}_{3,1}^* = \sum\nolimits_i \left(f_i - f_i^{eq}\right)\left(\mathbf{v}_i^*\cdot\mathbf{v}_i^* + \eta_i^2\right)\mathbf{v}_i^*, \tag{13}$$

$$\mathbf{\Delta}_3^* = \sum\nolimits_i \left(f_i - f_i^{eq}\right)\mathbf{v}_i^*\mathbf{v}_i^*\mathbf{v}_i^*, \tag{14}$$

$$\mathbf{\Delta}_{4,2}^* = \sum\nolimits_i \left(f_i - f_i^{eq}\right)\left(\mathbf{v}_i^*\cdot\mathbf{v}_i^* + \eta_i^2\right)\mathbf{v}_i^*\mathbf{v}_i^*. \tag{15}$$

The second order tensor $\mathbf{\Delta}_2^*$ corresponds to the viscous stress tensor and the nonorganized energy. The vector $\mathbf{\Delta}_{3,1}^*$ corresponds to the heat flux and

is related to the nonorganized energy flux. $\mathbf{\Delta}_3^*$ and $\mathbf{\Delta}_{4,2}^*$ are higher-order nonequilibrium quantities beyond traditional NS models. It is worth noting that comparing with the previous DBMs constructed in raw-moment space, the CDBM can provide the nonequilibrium effects related to the thermal fluctuation directly.

3. Verification and validation

In this section, we conduct several benchmark cases to verify the effectiveness and accuracy of the proposed CDBM for compressible flows. (1) The sound wave is simulated to verify that the CDBM is suitable for compressible flows. (2) The shock wave is carried out to demonstrate the CDBM has the capability of measuring supersonic flows and the corresponding nonequilibrium manifestations. (3) To verify the CDBM for adjustable specific heat ratios and Prandtl numbers, we simulate Couette flow. (4) Then, a typical two-dimensional benchmark, shock reflection, is simulated successfully. (5) Finally, a reacting wave is simulated in order to verify the suitability of CDBM for supersonic reactive flows. It should be noted that the second-order Runge-Kutta scheme is adopted for the time derivative in Eq. 1, and the second-order nonoscillatory and nonfree-parameter dissipation difference scheme is employed for the space derivatives [37].

3.1. Sound wave

Firstly, let us demonstrate that the CDBM is capable of capturing the sound wave. The initial condition is in a two-dimensional field with $(\rho, u_x, u_y, T) = (1, 0, 0, 1)$. For the computational domain, the grid mesh is $N_x \times N_y = 801 \times 801$, and the spatial step is $\Delta x = \Delta y = 5 \times 10^{-4}$. The temporal step is $\Delta t = 1 \times 10^{-5}$. A small perturbation $\rho = 1.0 + 0.01 \sin(t \times 2\pi/0.05)$ is imposed at the center. The perturbation spreads around at the speed of sound. Therefore, the length of the wave can be used to verify the accuracy of our model. The inflow and outflow boundary conditions are adopted. Figure 2 exhibits the pressure profile of the sound wave at time t=0.125. The theoretical value of the wave length is $l = 0.148$, while the simulation result is $l = 0.147$. It is evident that the relative error between the simulation result and the exact solution is 0.68%, which is satisfactory.

3.2. Shock wave

Now we consider a shock wave propagating from left to right. At the beginning, the shock front is located at $x = 0.01$ with a Mach number Ma =

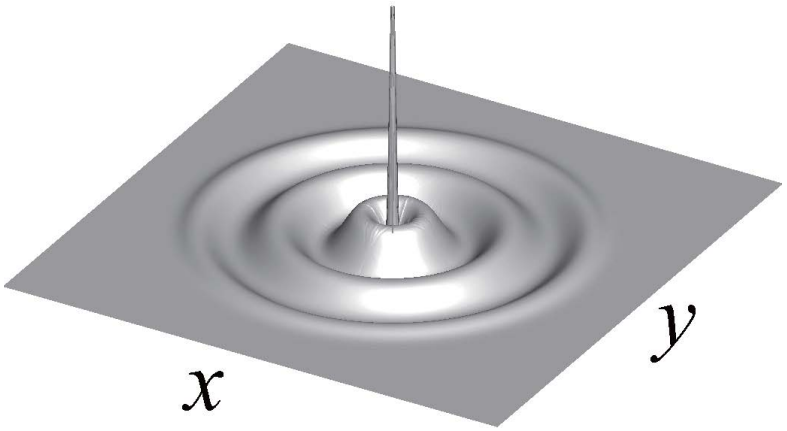

Figure 2: Propagation of the two-dimensional sound waves at time $t = 0.125$.

2. The initial state is set by the Hugoniot relation,

$$\begin{cases} (\rho, u_x, u_y, T)_L = (2.667, 1.479, 0, 1.688)\,, \\ (\rho, u_x, u_y, T)_R = (1, 0, 0, 1)\,, \end{cases} \tag{16}$$

where the subscripts L and R denote $0 < x \leq 0.01$ and $0.01 < x \leq 1$, respectively. In addition, inflow and outflow boundary conditions are employed in the x direction, and the periodic boundary condition is adopted in the y direction.

Grid convergence analysis is an important issue for numerical models, hence we carry out simulations of the shock wave with various spatial steps to verify the numerical accuracy. Figure 3 (a) plots density profiles of the shock wave at a time instant $t = 0.2$, the dash-dot-doted, dash-dotted, dotted, and dashed lines represent numerical results under spatial steps $\Delta x_1 = 2 \times 10^{-4}$, $\Delta x_2 = 1.414 \times 10^{-4}$, $\Delta x_3 = 1 \times 10^{-4}$, and $\Delta x_4 = 7.071 \times 10^{-5}$, respectively. The solid lines display the exact solution. The relative difference of the maximum value of $\Delta^*_{2,xx}$ around the shock wave is chosen as the numerical error. Figure 3 (b) illustrates the numerical error versus space step. The squares stand for the CDBM results and the line for the fitting function $\ln(error) = k \ln(\Delta x) + 14.79$. The slope is $k = 2$ which is equal to the exact value $k = 2$, since the space derivative is solved at the second order level. Besides, it is proved that the CDBM can capture the nonequilibrium effects effectively and precisely.

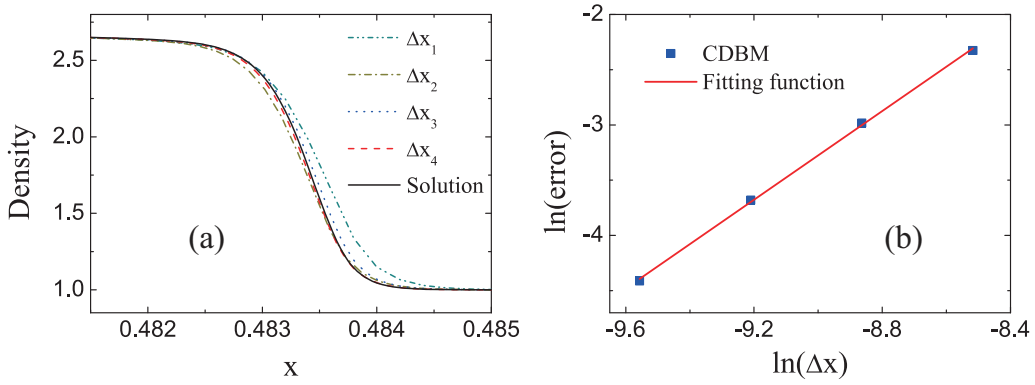

Figure 3: Grid convergence analysis: (a) profiles of density at a time instant t=0.2, (b) relative errors under various spatial steps.

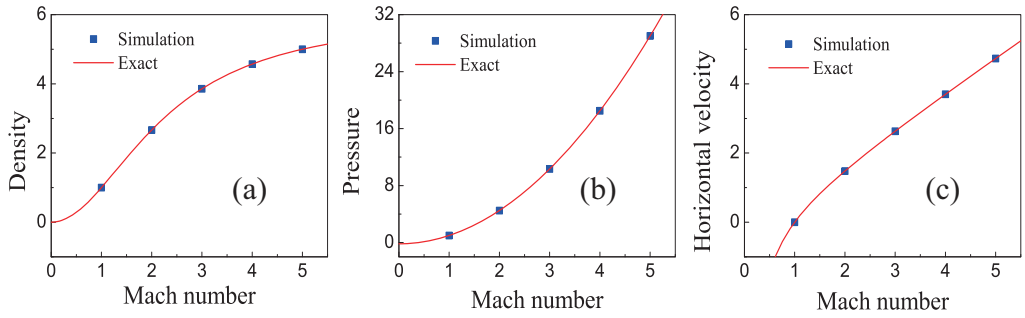

Figure 4: Profiles of density (a), pressure (b),and horizontal velocity (c) with various Mach numbers. Symbols represent CDBM results, and solid lines stand for exact solutions.

Then, we simulate a shock wave with various Mach numbers. The spatial step is $\Delta x = \Delta y = 1 \times 10^{-4}$, and the temporal step $\Delta t = 2.5 \times 10^{-6}$. Figure 4 display the profiles of (a) density, (b)pressure, and (c) horizontal velocity versus Mach number, respectively. The symbols show the simulation results and the solid lines indicate the exact solution,

$$\begin{cases} \rho = \frac{(\gamma+1)\mathrm{Ma}^2\rho_0}{(\gamma-1)\mathrm{Ma}^2+2}, \\ p = \frac{2\gamma p_0}{\gamma+1}\mathrm{Ma}^2 - \frac{\gamma-1}{\gamma+1}p_0, \\ u_x = \frac{2c_0}{\gamma+1}\left(\mathrm{Ma} - \frac{1}{\mathrm{Ma}}\right) + u_0. \end{cases} \tag{17}$$

It is evident that the simulation results coincide well with the theoretical val-

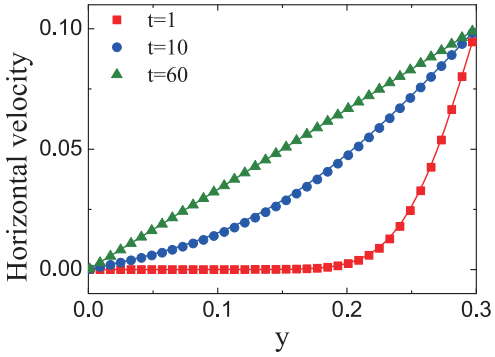

Figure 5: Distribution of horizontal velocity along y direction in the evolution of Couette flow at various time instants. The symbols indicate CDBM results and the lines denote exact solutions.

ues. Consequently, the CDBM is suitable for high Mach number supersonic compressible flows.

3.3. Thermal Couette flow

In this subsection, the simulation of Couette flow is carried out to demonstrate that the CDBM is applicable to thermal flow with flexible specific heat ratios and Prandtl numbers. The initial state of the fluid is $\rho_0 = 1.0$, $T_0 = 1.0$, and $\mathbf{u}_0 = 0$. Below the flow is a wall keeping still with a fixed temperature $T_1 = 1.0$, above the flow is a plate moving rightwards with constant speed $u_2 = 0.1$ and temperature $T_2 = 1.0$. The viscous shear stress transmits momentum into the fluid and changes the flow velocity distribution. The height between the walls is $H = 0.3$. The temporal step is $\Delta t = 10^{-4}$, and the spatial step is $\Delta x = \Delta y = 10^{-3}$. Periodic boundary conditions are applied to the left and right boundaries, and the nonequilibrium extrapolation method is employed for the bottom and top boundaries.

Figure 5 indicates the horizontal velocity versus y at times t=1, 10, and 60, respectively. The symbols represent the simulation results, and the lines for the analytical solutions,

$$u = \frac{y}{H}u_0 + \frac{2}{\pi}u_0 \sum_{n=1}^{\infty}\left[\frac{(-1)^n}{n} exp\Big(-n^2\pi^2\frac{\mu t}{\rho H^2}\Big)\sin\Big(\frac{n\pi y}{H}\Big)\right]. \qquad (18)$$

Figure 6 (a) illustrates the temperature profiles when the Couette flow reaches equilibrium with various specific heat ratios $\gamma = 1.5$, 1.28, and 1.18,

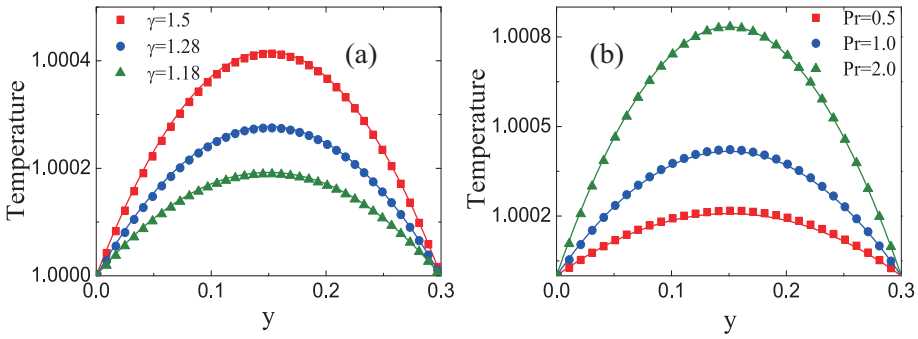

Figure 6: Temperature distribution along the y direction with various specific heat ratios (a). Temperature distribution along the y direction with various Prandtl numbers (b) The symbols indicate CDBM results and the lines denote exact solutions.

respectively. Similarly, the symbols denote CDBM results, and the lines stand for the exact solutions. Theoretically, the distribution of temperature in the y direction follows

$$T = T_1 + (T_2 - T_1)\frac{y}{H} + \frac{\mu}{2\kappa}u_0^2\frac{y}{H}(1 - \frac{y}{H}), \tag{19}$$

where $T_1 = 1.0$ and $T_2 = 1.0$ are temperatures of the lower and upper walls, respectively. Here μ and κ are the dynamic viscosity and thermal conductivity, respectively. Moreover, the dynamic viscosity and thermal conductivity take the form, $\mu = p/S_\mu$ and $\kappa = (D + I + 2)\,p/(2S_\kappa)$, under the conditions $S_5 = S_6 = S_7 = S_\mu$ and $S_8 = S_9 = S_\kappa$. Obviously, the simulation results agree well with the analytical solutions. Hence, the CDBM has the capability of capturing the flow field with various specific heat ratios in the dynamic process of the Couette Flow. Similarly, Fig 6 (b) demonstrates the distribution of temperature along y direction in the evolution of Couette flow at various Prandtl numbers. The collision parameters are $S_\kappa = 10^3$, with $S_\mu = 2 \times 10^3$, 10^3, and 5×10^2 for Pr = 0.5, 1.0, and 2.0, respectively. It is clear that our simulation results agree well with the analytical solutions for various Prandtl numbers.

For the purpose of demonstrating that the CDBM has the capability of capturing the nonequilibrium effects in the iterative process dynamically, we examine the nonequilibrium quantities $\Delta^*_{2,xy}$ and $\Delta^*_{3,1,y}$ in the case with $\gamma =$ 1.5. Figure 7 plots the CDBM results (symbols) at time instants $t = 1.0$, 10.0,

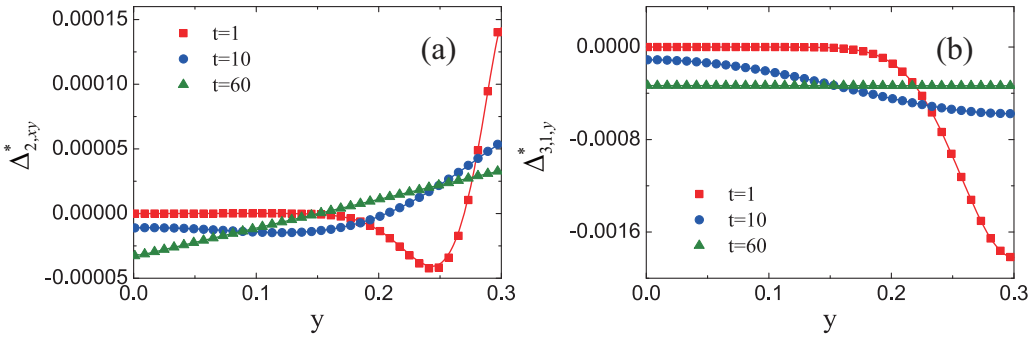

Figure 7: Vertical distribution of $\Delta^*_{2,xy}$ and $\Delta^*_{3,1,y}$ at time instants $t = 1.0$, 10.0, and 60.0, respectively. Symbols denote the CDBM results, lines denote the corresponding theoretical solutions.

and 60.0, respectively. And the lines are corresponding analytic solutions,

$$\Delta^*_{2,xy} = -\mu \left(\frac{\partial u_x}{\partial y} + \frac{\partial u_y}{\partial x} \right), \tag{20}$$

$$\Delta^*_{3,1,y} = -\kappa \frac{\partial T}{\partial y}. \tag{21}$$

It can be found that the CDBM results are in good agreement with the analytical values. That is to say, the CDBM could describe the nonequilibrium behaviours accurately.

3.4. Shock reflection

For the purpose of verifying the model for two-dimensional systems, we use a typical benchmark: regular shock reflection. The computational domain is a rectangle. The reflecting surface is imposed on the bottom, the supersonic outflow is adopted for the right boundary, and the Dirichlet conditions are utilized on the top and left boundaries, i.e.,

$$\begin{cases} (\rho, u_x, u_y, T)_{0,y,t} = (1, 2, 0, 0.5)\,, \\ (\rho, u_x, u_y, T)_{x,0.1,t} = (1.25, 1.9, -0.173, 0.56)\,, \end{cases} \tag{22}$$

The parameters are $N_x \times N_y = 300 \times 100$, $\Delta x = \Delta y = 1 \times 10^{-4}$, and $\Delta t = 5 \times 10^{-6}$. Figure 8 exhibits the density contour of the steady regular shock reflection. Theoretically, the angle between the incident shock wave and the wall is $\alpha = \pi/6$, while the CDBM gives the angle $\alpha = \mathrm{ArcTan}(0.1/0.175)$. The relative difference between them is only 0.8%, which is satisfying.

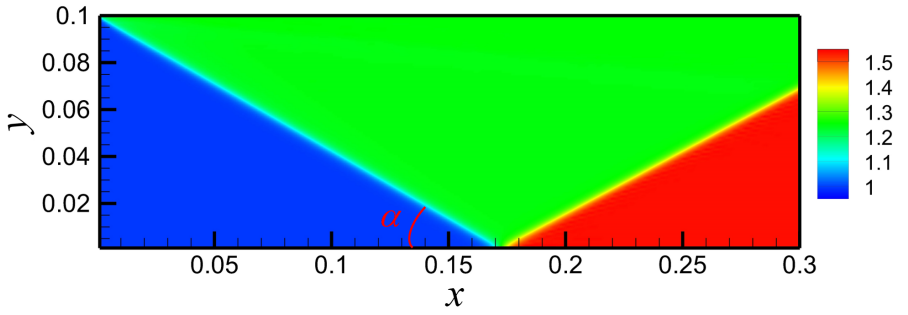

Figure 8: Density contour of steady regular shock reflection on a wall.

3.5. Supersonic reacting wave

Finally, for the sake of verifying its suitability for supersonic reactive flows, the model is used to simulate a reacting wave. Here, the two-step reaction scheme is employed to control the chemical reaction process [38]. The initial field is divided into two parts, with the reacting wave travels from left to right. The initial configuration satisfies the following Rankine-Hugoniot conditions

$$\begin{cases} (\rho, u_x, u_y, T)_L = (1.3884, 0.5774, 0, 1.5786)\,, \\ (\rho, u_x, u_y, T)_R = (1, 0, 0, 1)\,, \end{cases} \tag{23}$$

where the subscript L and R indicate $0 \leq x \leq 0.05$ and $0.1 < x \leq 0.5$, respectively. The Mach number is 1.74. The other parameters are $\Delta x = \Delta y = 1 \times 10^{-5}$, and $\Delta t = 2 \times 10^{-6}$ to ensure a high resolution. In addition, inflow and outflow boundary conditions are employed in the x direction, and the periodic boundary condition is adopted in the y direction.

Figure 9 displays the wave profiles (a) density, (b) temperature, (c) horizontal velocity and (d)pressure. The symbols stand for the CDBM results, and the solid lines stand for the solutions of the Zel'dovich-Neumann-Döring (ZND) theory [39]. Clearly the results of the current model agree well with the ZND solutions. Compared with the ZND solutions $(\rho, u_x, u_y, T, P) = (1.3884, 0.5774, 0, 1.5786, 2.1916)$ behind the detonation wave, the simulation results behind the wave are $(\rho, u_x, u_y, T, P) = (1.3883, 0.5778, 0, 1.5785, 2.1914)$. The relative errors are 0.007%, 0.06%, 0%, 0.006% and 0.009% respectively, which demonstrates that the CDBM is able to simulate the supersonic reactive flows accurately.

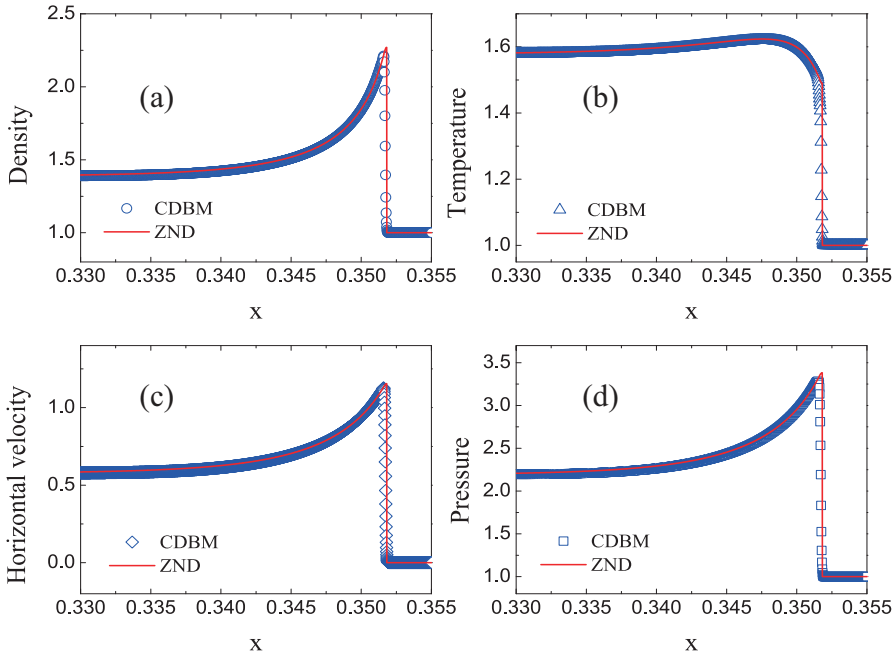

Figure 9: Profiles of a supersonic reacting wave: (a) density, (b) temperature, (c) horizontal velocity and (d) pressure. The symbols represent the simulation results, the solid lines represent ZND solutions.

4. Conclusions and Discussions

In this paper, we present the development of a CDBM capable of accurately simulating compressible reactive flows. The governing equations are a unified set of kinetic equations discretized in velocity space with reaction source terms describing the influence of the chemical reaction. In the framework of the CDBM, the central kinetic moments are adopted to calculate the discrete equilibrium distribution functions, collision terms and reaction terms with utilization of a matrix inversion method. Via the Chapman-Enskog expansion, the macroscopic quantities and noneuilibrium effects beyond the conventional hydrodynamic governing equations are described by central moment relationships which are based on the peculiar motion. Notably, unlike all previous DBMs, the CDBM no longer necessitates an additional term, rendering it consistent with NS equations in the hydrodynamic limit during the coarse-grained modeling process. Moreover, the CDBM can directly quantify the nonequilibrium effects related to the thermal fluctuation, which is different from previous DBMs constructed in raw-moment space. To validate the performance of the present model, the accuracy in capturing compressible waves is initially assessed by simulating a sound wave. Subsequently, the model's capability to simulate supersonic flows is demonstrated through shock wave benchmarks, with concurrent verification of grid convergence analysis. Besides, the thermal couette flows are employed to demonstrated that the specific heat ratio and Prandtl number are adjustable in CDBM. Moreover, successful simulation of a typical two-dimensional benchmark, shock reflection, is accomplished. Lastly, a supersonic reactive wave is employed to demonstrate that the influence of chemical reactions can be characterized by CDBM.

Acknowledgements. This work is supported by Guangdong Basic and Applied Basic Research Foundation (under Grant No. 2022A1515012116) and China Scholarship Council (Nos. 202306380179 and 202306380288). Support from the UK Engineering and Physical Sciences Research Council under the project "UK Consortium on Mesoscale Engineering Sciences (UKCOMES)" (Grant No. EP/X035875/1) is gratefully acknowledged. This work made use of computational support by CoSeC, the Computational Science Centre for Research Communities, through UKCOMES.

References

[1] E. S. Oran, J. P. Boris, J. P. Boris, Numerical simulation of reactive flow, Vol. 2, Citeseer, 2001.

[2] N. Peters, Turbulent combustion, Measurement Science and Technology 12 (11) (2001) 2022–2022.

[3] T. Poinsot, D. Veynante, Theoretical and numerical combustion, RT Edwards, Inc., 2005.

[4] E. Nagnibeda, E. Kustova, Non-equilibrium reacting gas flows: kinetic theory of transport and relaxation processes, Springer Science & Business Media, 2009.

[5] S. Succi, G. Bella, F. Papetti, Lattice kinetic theory for numerical combustion, Journal of Scientific Computing 12 (1997) 395–408.

[6] O. Filippova, D. Hänel, A novel lattice bgk approach for low mach number combustion, Journal of Computational Physics 158 (2) (2000) 139–160.

[7] K. Yamamoto, X. He, G. D. Doolen, Simulation of combustion field with lattice boltzmann method, Journal of statistical physics 107 (2002) 367–383.

[8] K. Yamamoto, N. Takada, M. Misawa, Combustion simulation with lattice boltzmann method in a three-dimensional porous structure, Proceedings of the Combustion Institute 30 (1) (2005) 1509–1515.

[9] S. Chen, Z. Liu, C. Zhang, Z. He, Z. Tian, B. Shi, C. Zheng, A novel coupled lattice boltzmann model for low mach number combustion simulation, Applied Mathematics and Computation 193 (1) (2007) 266–284.

[10] S. Chen, Z. Liu, Z. Tian, B. Shi, C. Zheng, A simple lattice boltzmann scheme for combustion simulation, Computers & Mathematics with Applications 55 (7) (2008) 1424–1432.

[11] E. Chiavazzo, I. V. Karlin, A. N. Gorban, K. Boulouchos, Coupling of the model reduction technique with the lattice boltzmann method for combustion simulations, Combustion and Flame 157 (10) (2010) 1833–1849.

[12] S. A. Hosseini, P. Boivin, D. Thévenin, I. Karlin, Lattice boltzmann methods for combustion applications, Progress in Energy and Combustion Science 102 (2024) 101140.

[13] S. A. Hosseini, H. Safari, N. Darabiha, D. Thévenin, M. Krafczyk, Hybrid lattice boltzmann-finite difference model for low mach number combustion simulation, Combustion and Flame 209 (2019) 394–404.

[14] N. Sawant, B. Dorschner, I. V. Karlin, Consistent lattice boltzmann model for reactive mixtures, Journal of Fluid Mechanics 941 (2022) A62.

[15] G. Wissocq, S. Taileb, S. Zhao, P. Boivin, A hybrid lattice boltzmann method for gaseous detonations, Journal of Computational Physics 494 (2023) 112525.

[16] Y. Gan, A. Xu, G. Zhang, S. Succi, Discrete Boltzmann modeling of multiphase flows: hydrodynamic and thermodynamic non-equilibrium effects, Soft Matter 11 (26) (2015) 5336–5345.

[17] H. Lai, A. Xu, G. Zhang, Y. Gan, Y. Ying, S. Succi, Nonequilibrium thermohydrodynamic effects on the Rayleigh–Taylor instability in compressible flows, Phys. Rev. E 94 (2) (2016) 023106.

[18] C. Lin, A. Xu, G. Zhang, Y. Li, Double-distribution-function discrete Boltzmann model for combustion, Combust. Flame 164 (2016) 137–151.

[19] C. Lin, X. Su, Y. Zhang, Hydrodynamic and Thermodynamic Nonequilibrium Effects around Shock Waves: Based on a Discrete Boltzmann Method, Entropy 22 (12) (2020) 1397.

[20] L. Chen, H. Lai, C. Lin, D. Li, Specific heat ratio effects of compressible Rayleigh—Taylor instability studied by discrete Boltzmann method, Front. Phys. 16 (5) (2021) 1–12.

[21] Z. Liu, J. Song, A. Xu, Y. Zhang, K. Xie, Discrete boltzmann modeling of plasma shock wave, Proceedings of the Institution of Mechanical Engineers, Part C: Journal of Mechanical Engineering Science 237 (11) (2023) 2532–2548.

[22] X. Su, C. Lin, Unsteady detonation with thermodynamic nonequilibrium effect based on the kinetic theory, Communications in Theoretical Physics (2023).

[23] A. Xu, Y. Shan, F. Chen, Y. Gan, C. Lin, Progress of mesoscale modeling and investigation of combustion multiphase flow, Acta Aeronaut. Astronaut. Sin. 42 (12) (2021) 625842.

[24] A. Xu, G. Zhang, Y. Gan, F. Chen, X. Yu, Lattice Boltzmann modeling and simulation of compressible flows, Front. Phys. 7 (5) (2012) 582–600.

[25] B. Yan, A. Xu, G. Zhang, Y. Ying, H. Li, Lattice Boltzmann model for combustion and detonation, Front. Phys. 8 (1) (2013) 94–110.

[26] C. Lin, A. Xu, G. Zhang, Y. Li, S. Succi, Polar-coordinate lattice Boltzmann modeling of compressible flows, Phys. Rev. E 89 (2014) 013307.

[27] A. Xu, C. Lin, G. Zhang, Y. Li, Multiple-relaxation-time lattice Boltzmann kinetic model for combustion, Phys. Rev. E 91 (2015) 043306.

[28] Y. Zhang, A. Xu, G. Zhang, C. Zhu, C. Lin, Kinetic modeling of detonation and effects of negative temperature coefficient, Combust. Flame 173 (2016) 483–492.

[29] Y. Ji, C. Lin, K. H. Luo, Three-dimensional multiple-relaxation-time discrete Boltzmann model of compressible reactive flows with nonequilibrium effects, AIP Adv. 11 (4) (2021) 045217.

[30] Y. Ji, S. A. Hosseini, B. Dorschner, K. H. Luo, I. V. Karlin, Eulerian discrete kinetic framework in comoving reference frame for hypersonic flows, J. Fluid Mech. 983 (2024) A11.

[31] M. Geier, A. Greiner, J. G. Korvink, Cascaded digital lattice boltzmann automata for high reynolds number flow, Physical Review E 73 (6) (2006) 066705.

[32] D. Lycett-Brown, K. H. Luo, R. Liu, P. Lv, Binary droplet collision simulations by a multiphase cascaded lattice boltzmann method, Physics of Fluids 26 (2) (2014).

[33] L. Fei, K. H. Luo, C. Lin, Q. Li, Modeling incompressible thermal flows using a central-moments-based lattice boltzmann method, International Journal of Heat and Mass Transfer 120 (2018) 624–634.

[34] C. Zhang, L.-P. Wang, H. Liang, Z. Guo, Central-moment discrete unified gas-kinetic scheme for incompressible two-phase flows with large density ratio, Journal of Computational Physics 482 (2023) 112040.

[35] C. Lin, A. Xu, G. Zhang, K. H. Luo, Y. Li, Discrete Boltzmann modeling of Rayleigh–Taylor instability in two-component compressible flows, Phys. Rev. E 96 (2017) 053305.

[36] A. Xu, C. Lin, G. Zhang, Y. Li, Multiple-relaxation-time lattice boltzmann kinetic model for combustion, Physical Review E 91 (4) (2015) 043306.

[37] H. Zhang, F. Zhuang, NND schemes and their applications to numerical simulation of two-and three-dimensional flows, Advances in Applied Mechanics 29 (1991) 193–256.

[38] H. Ng, M. Radulescu, A. Higgins, N. Nikiforakis, J. Lee, Numerical investigation of the instability for one-dimensional chapman–jouguet detonations with chain-branching kinetics, Combustion Theory and Modelling 9 (3) (2005) 385–401.

[39] C. K. Law, Combustion physics, Cambridge University Press, Cambridge, 2006.